SOFT ROBOTICS
Volume 00, Number 00, 2026
Mary Ann Liebert, A Part of Sage
© Mary Ann Liebert (NY), LLC
DOI: 10.1177/21695172261420664

ORIGINAL ARTICLE

Monolithically Printed Pneumatic Proprioceptive Actuator with Integrated Optical Waveguide Using a Single Material

Shaowu Tang,[1–3] Xiaohuang Liu,[2] Zhonggui Fang,[4] Yige Wu,[2] Juan Yi,[5] Zheng Wang,[4] Jian S. Dai,[2]
and Sicong Liu[1]

Abstract

In muscle tissues, muscle fibers generate active force, muscle spindles provide passive proprioceptive feedback, and connective tissues tightly bind their movements together, forming a reliable biological system. Inspired by this, we propose a single material fabrication method to monolithically print pneumatic proprioceptive actuators (MPPPAs). By leveraging the multifunctional properties of thermoplastic polyurethane (TPU), including inherent flexibility, fusibility, and translucency, and employing a desktop-level fused deposition modeling printer, airtight chambers and embedded optical waveguides are realized within a continuous printing process. Optimized printing parameters lead to fully densified chambers, resulting in a leakage rate of only 0.85% under 200 kPa and maintaining 462.55 kPa after 10 minutes from an initial 500 kPa. The optical waveguides exhibit robust proprioception, maintaining a stable signal over 5000 bending cycles with less than 0.5% drift. Mechanical tests confirm synchronized deformation and continuous structural integration across the monolithically co-printed actuator-sensor region, enabling MPPPAs to achieve reliable actuation-sensing performance with sensing errors below 1.82%. Demonstrations include precise surface contour measurement with the root mean square error of 0.16 mm and real-time gripping width estimation, validating the method's effectiveness in fabricating compact and stable proprioceptive actuators. This research advances actuation-sensing integration in soft robotics, enabling streamlined fabrication and improved reliability for future intelligent systems.

Keywords: soft robotics, integrated actuation and sensing, single material printing, proprioceptive actuators, optical waveguides

Introduction

Over the past decades, soft pneumatic actuators (SPAs) have attracted widespread attention due to their low cost and weight, fast response, and easy implementation[1,2] and have been widely investigated in applications such as gripping,[3] locomotion,[4,5] and wearable devices[6,7] to address various practical challenges. Among them, pneumatic proprioceptive actuators (PPAs), which can reliably perceive their own deformation state, have demonstrated superior accuracy and stability in task execution by leveraging proprioceptive feedback.[8,9]

From both functional and structural perspectives, actuation and proprioception represent the two core subsystems of PPAs. The overall performance of PPAs depends not only on the independent performance of the actuators and sensors but also critically on their effective integration.[10] Consequently, extensive research efforts have been devoted to combining and coupling these subsystems through methods such as noncontact installation, attached or embedded assembly, and monolithic 3D printing.

Among these integration methods, noncontact installation typically relies on commercially available contactless sensors to capture deformation information without direct physical connection to the soft actuators.[11] This approach provides a straightforward way to realize PPAs, as it effectively avoids the challenges associated with the continuous and complex

---

[1] Sino-German College of Intelligent Manufacturing, Shenzhen Technology University, Pingshan, China.
[2] Department of Mechanical and Energy Engineering, Southern University of Science and Technology, Shenzhen, China.
[3] Department of Aerospace and Mechanical Engineering, University of Southern California, Los Angeles, California, United States.
[4] Wisson Robotics, Shenzhen, China.
[5] School of Advanced Engineering, Great Bay University, Dongguan, Guangdong, China.

deformations of soft actuator materials.[12,13] For instance, high-speed cameras can capture local or global deformations through heatmap analysis;[14] external magnetic fields can track the pose of the actuator tip;[15] and high-precision laser sensors[16,17] or air pressure sensors[18,19] can provide efficient feedback on the deformation of linear actuators. However, these noncontact sensing methods often require bulky and expensive external equipment, which limits the suitability of PPAs in applications demanding low cost, portability, and flexibility.

In contrast, flexible and stretchable sensors offer a more reliable approach to capturing continuous actuator deformation, owing to advantages such as enhanced resistance to interference, multimodal sensing capabilities, and compatibility with compact integration.[20–22] By attaching or embedding these sensors directly onto or within the actuators, sensor deformation becomes mechanically coupled with actuator deformation, resulting in more stable proprioceptive feedback.[23,24] Recent studies have shown that thin-film soft sensors distributed across actuator surfaces can reconstruct kinematic geometry[25–27]; slender optical waveguides embedded within bending actuators can detect bending motion, enabling proprioceptive functions similar to human fingers[28–32]; and multiple sensor types can be combined to achieve multimodal deformation sensing.[33,34] However, these assembly-based methods inevitably involve labor-intensive manual integration processes, which can introduce installation errors and compromise consistency and repeatability. Bioinspired somatosensory actuators leverage the multifunctional characteristics of smart materials to achieve integrated actuation and sensing without the need for assembly. However, they still require complex material synthesis and fabrication processes.[35,36]

State-of-the-art research has explored multimaterial 3D printing technologies as an innovative method to develop PPAs,[37] due to their capabilities to fabricate complex geometries, enable customized integration, and support multiscale manufacturing.[38,39] Researchers have successfully employed 3D printing to individually fabricate soft actuators with diverse structures,[40–42] high-performance sensors, or sensor arrays[43–45] and have also monolithically realized PPAs by integrating actuators and sensors into a single printed body.[46–49] For example, three matrix materials and two ink materials were combined through 12 printing steps to achieve actuation and sensing capabilities;[50] conductive silicone has been used to fabricate actuators with complex cavity structures coupled with flexible triboelectric sensors;[51] and sensor-embedded soft grippers have been monolithically printed by using materials with different physical and chemical properties.[37] These studies represent significant advances toward streamlined fabrication of complex, multifunctional PPAs.

However, several unavoidable challenges remain. On one hand, mismatches in mechanical properties such as hardness and stiffness among different materials can lead to stress concentrations during the synchronous movement of sensors and actuators,[9,52] thereby weakening the bonding interfaces and limiting overall performance. On the other hand, the multimaterial printing method imposes stringent requirements on material compatibility and the printer's capability to process multiple materials, often necessitating expensive equipment and intricate procedures such as material switching and system calibration.[37,50]

In this work, to address the challenges integrating actuation and sensing in PPAs, we investigate the multifunctional properties of a single material and leverage its inherent versatility to monolithically realize both actuation and sensing capabilities within a continuous printed structure. This strategy fundamentally mitigates issues arising from mismatched mechanical properties in multimaterial devices. Furthermore, achieving such integration solely with a single material and commercially available desktop-level equipment constitutes a substantial advancement in monolithic fabrication techniques for proprioceptive soft actuators.

The main contributions are summarized as follows:

1) Inspired by the multifunctionality of the muscle tissue, we propose a method that leverages the multifunctional properties of a single material to monolithically print pneumatic proprioceptive actuators (MPPPAs). This approach enables the actuator and sensing regions to share uniform mechanical properties and maintain seamless structural continuity throughout the printed device.
2) A commercially available TPU filament is investigated for its multifunctional properties, including flexibility, fusibility, and translucency. By exploiting these properties and employing a conventional desktop-level fused deposition modeling (FDM) printer, we develop optimized printing parameters to fabricate both airtight chamber walls for actuation and optical waveguides for sensing from a single TPU material. The feasibility of constructing the integrated actuation and sensing functions is validated through experiments and simulations.
3) Building on this single-material printing approach and the multifunctional properties of the TPU filament, MPPPAs that integrate both actuation and sensing regions are fabricated monolithically and continuously in a single uninterrupted printing process through optimized printing parameters. Experimental results demonstrate that the resulting MPPPAs exhibit stable and reliable actuation performance, along with superior proprioceptive sensing capabilities.

Materials and Methods

Design concept of MPPPA

The concept of the MPPPA refers to a proprioceptive actuator that integrates both actuation and sensing capabilities within its body, fabricated using a single material through monolithic 3D printing. It is inspired by the muscle tissue, shown in Figure 1A, which comprises muscles, muscle spindles, and connective tissue. When the human body performs movement tasks, the brain first sends activation signals to the muscles via the spinal cord, causing them to contract and produce motion. Meanwhile, due to the tight coupling of muscles and muscle spindles by connective tissue, this active contraction passively deforms the muscle spindles. Acting as proprioceptors, the muscle spindles detect these deformations and transmit sensory feedback to the brain, thereby establishing a closed-loop system that integrates actuation with proprioceptive sensing.[53,54] Excluding neural regulation by the brain, this sophisticated proprioceptive mechanism primarily relies on three structural and mechanical conditions. First, coordinated actuation and sensing, in which muscle fibers generate movement while muscle spindles provide sensory information. Second, strong mechanical coupling through connective tissue ensures synchronized deformation between muscle fibers and muscle spindles. Third, closely matched mechanical properties among muscle fibers, spindles, and connective tissue, which help reduce stress concentrations during overall tissue deformation.[55–57]

This delicately balanced and highly integrated biological model guides our design and fabrication method for proprioceptive actuators, as shown in Figure 1B–E. Specifically, we utilize a commercially available TPU filament and its multifunctional properties to fabricate both actuation and sensing components using a standard single-nozzle FDM printer (Raise3D Pro2 Plus, Supplementary Fig. S1), combined with tailored printing parameters and toolpaths. This includes harnessing the flexibility and fusibility of TPU to print soft, airtight pneumatic chambers (Fig. 1C) and leveraging its flexibility and translucency to print soft optical waveguides (Fig. 1D). Furthermore, as shown in Figure 1E, by embedding the waveguide inside the actuator through an integrated design and adjusting specific printing parameters, we achieve the monolithic fabrication of pneumatic proprioceptive actuators embedded with optical waveguides (Supplementary Movie S1). Since the proposed concept fabricates both the actuator and the waveguide using the same material, the fused deposition process results in continuous molecular entanglement throughout the printed structure, promoted by high-temperature melting and subsequent solidification.[58,59] This process ensures uniform mechanical properties throughout the actuator and waveguide regions and enables synchronized global and local deformation within the monolithic structure.

Overall, the proposed concept of MPPPAs is inspired by the structure and mechanical mechanism of human muscle tissue and leverages the multifunctional properties of TPU material. Using a common FDM printer and specifically designed printing parameters, it enables the monolithic fabrication of compact proprioceptive actuators. Therefore, the proposed method successfully replicates the structural and mechanical conditions underlying the sophisticated, robust, and stable functionality of the human muscle tissue system. In the following sections, we present and discuss the design, fabrication, and performance of the printed actuator, optical waveguide, and integrated proprioceptive actuator, and further illustrate their potential applications through a surface reconstruction demonstration.

Fabrication and characterization of MPPPA

3D printing of actuators, waveguides, and test psamples. All soft actuators, optical waveguides, and test samples in this study were fabricated using a commercial TPU filament (PolyFlex™ TPU90, clear color, Polymaker) with an FDM 3D printer (Raise3D Pro2 Plus, Raise3D Technologies, Inc.). Printing parameters and toolpaths were configured via commercial slicing software (ideaMaker 5.1.4, Raise3D Technologies, Inc.). To slice the actuator and waveguide regions with

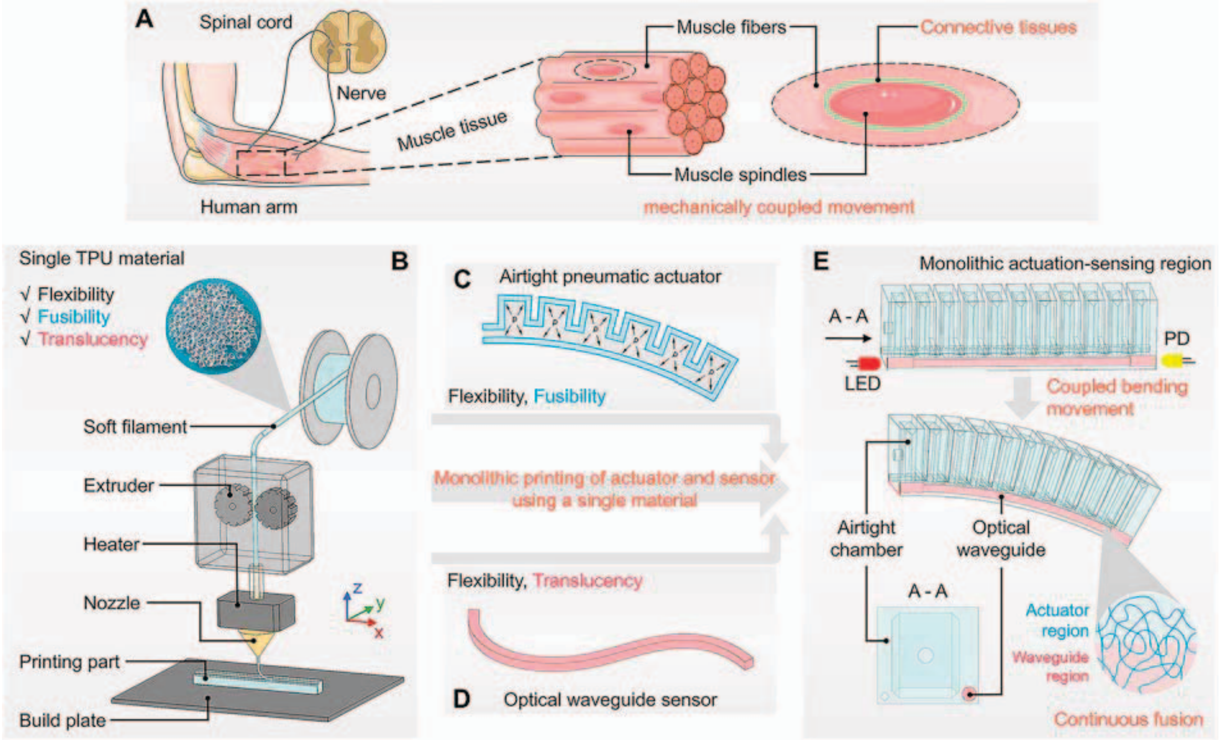

FIG. 1. Overview of the proposed concept, including the biological mechanism of muscle tissue, the multifunction properties of TPU material, and the monolithic printing method for MPPPAs. **(A)** The biological mechanism of proprioceptive muscle tissue illustrates the tight bonding between muscle fibers and muscle spindles through connective tissue. Inspired by this, **(B)** we utilize FDM technology and the multifunctionality of a clear TPU filament to monolithically print **(C)** airtight pneumatic actuators, **(D)** optical waveguide sensors, and **(E)** integrated MPPPAs with continuous fusion regions. MPPPA, monolithically print pneumatic proprioceptive actuators, FDM, fused deposition modeling.

different printing parameters, two slicing groups were created in ideaMaker, as shown in Supplementary Figure S18. Since moisture absorption is a common issue for TPU filaments exposed to ambient air, the filament was stored in a drying chamber (eBOX Lite, eSUN) to ensure consistent and reliable printing quality.

Optical sensing circuits. The optical waveguide sensor comprises a light-emitting diode (LED) (TSAL4400, Vishay Semiconductors) serving as the light source and a photodiode (PD) (TEFT 4300, Vishay Semiconductors) functioning as the receiver that converts incident light into an electrical signal. Both devices exhibit peak emission and response wavelengths of approximately 940 nm. To ensure stable and reliable sensing signals, the sensing circuit incorporates a voltage regulation module (based on the AMS1117-1.5 chip) that supplies a constant 1.5 V to the LED, as well as a signal amplification module (based on the INA180A2IDBVR chip) that amplifies the current signal generated by the PD and converts it into a 0–5 V voltage output (Supplementary Fig. S14). Capacitors C1 and C2 were each set to 100 nF; resistor R1 was configured as a variable resistor with an adjustable range of 0–20 Ω, and resistor R2 was a fixed resistor with a value of 75 Ω.

Sensor signal acquisition and data processing. The sensing signals used in the experiments primarily included pneumatic pressure measured by a pressure sensor (XGZP6857A, maximum 700 kPa, CFSensor Inc.), bending angle obtained from an inertial measurement unit (IMU, MPU6050, InvenSense Inc.), and voltage signals from the optical waveguide sensor. All signals were recorded in real time during actuation. The real-time data from these three types of sensors were acquired and transmitted to the microcontroller unit (MCU) via an analog-to-digital converter module board (AD7606, Analog Devices Inc.). The MCU then relayed all collected data to a PC through a serial interface for centralized acquisition. Subsequently, all data were processed and analyzed using MATLAB R2023a and Origin 2024 to generate the final results and figures.

Results

3D printing airtight chambers

The airtight chamber is a critical structural component of MPPPAs, and ensuring adequate airtightness is essential for achieving reliable actuation and consistent pressure regulation. In this section, we examine the airtightness of 3D printed chambers and explore strategies to enhance their ability to maintain stable internal pressure.

As an additive manufacturing technique, 3D printing produces chamber walls whose airtightness depends not only on the material's intrinsic densification properties but also directly on the specifics of the fabrication process. Previous studies have demonstrated that simplifying the chamber geometry and adopting continuous, closed Eulerian printing paths can effectively improve airtightness.[41] Robots employing this strategy were even able to operate stably under internal pressures of up to 138 kPa.[60] Motivated by these findings, and with the goal of further improving the high-pressure tolerance and actuation performance of 3D-printed structures, we systematically investigated and analyzed their microstructural characteristics and mechanical performance under different FDM printing parameters.

When constructing buildings with bricks, rectangular bricks are typically used to ensure dense packing and structural stability. In contrast, FDM printers typically use circular nozzles, which cause the extruded filament to naturally assume a cylindrical shape. This nonrectangular cross-section leads to air holes between adjacent printing paths (Fig. 2A). Although partial overlaps between paths facilitate the formation of molecular chains that enhance interlayer bonding, these holes still affect the internal stress distribution within the printed object, ultimately compromising its overall mechanical performance and airtightness.[58,59]

To achieve a dense printed structure, as shown in the lower part of Figure 2A, the actual extruded cross-sectional area must exceed the area of the dashed rectangular boundary ($A \geq h \times w$). Based on Supplementary Note S1 and Supplementary Table S1, a straightforward calculation shows that the printing parameters q should exceed 110% when $h = 0.1$ mm and should exceed 117% when $h = 0.2$ mm.

To validate the aforementioned model for eliminating micro-holes and to identify the optimal airtight-printing parameters for the MPPPA chamber region, several rectangular chamber samples (Supplementary Fig. S2) were fabricated using different printing parameter combinations and subsequently evaluated through airtightness testing. These samples were subsequently sectioned and examined via scanning electron microscopy (SEM) analysis. The surface morphology of the printed microstructures was characterized using a field-emission scanning electron microscope (GeminiSEM 360, ZEISS). Prior to imaging, the samples were sputter-coated with a thin layer of gold to improve conductivity. Representative SEM images are shown in Figure 2B and C, where the cross-sectional regions of the samples are magnified by 20× to highlight their internal structural features. In these images, the gray regions correspond to extruded TPU material, while the black regions indicate air holes. Specifically, when the layer height was set to 0.2 mm and the flow rate to 90%, the printed sample exhibited periodically arranged micro-holes, with a limited bonding area between adjacent extrusion paths. In contrast, reducing the layer height to 0.1 mm and increasing the flow rate to 110% resulted in excess extruded filament being compressed and spread during printing, effectively eliminating these holes. As shown in Figure 2C, the sample printed with a 0.1 mm layer height and 110% flow rate exhibits a fully dense TPU microstructure with no internal holes, effectively reducing stress concentrations and improving airtightness. Consistent with this observation, the mechanical test results in Supplementary Figures S3-S8 confirm that lower layer heights and higher flow rates yield more stable and superior mechanical performance. Therefore, a 0.1 mm layer height and 110% flow rate were selected for fabricating the airtight chamber region in all final MPPPA prototypes. In addition to these two key parameters, the other main printing settings used for chamber fabrication are summarized in Supplementary Table S1.

To verify the airtightness of chambers fabricated with these optimized parameters, preliminary tests were conducted on rectangular chambers, as shown in Figure 2D. Each chamber had dimensions of 35 mm × 19 mm × 20 mm and a wall thickness of 1.6 mm. The slicing path design consists of four

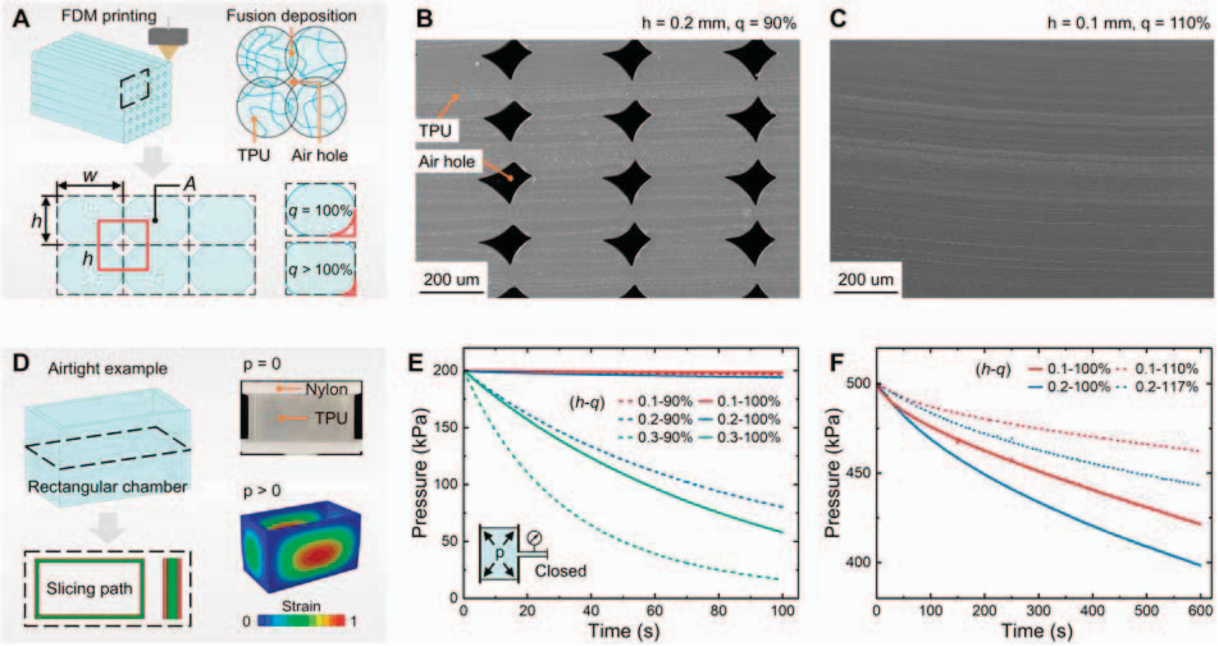

FIG. 2. Influence of 3D printing parameters on airtightness of printed objects. **(A)** The circular nozzle of the FDM printer creates holes between adjacent paths, which can be controlled by adjusting the printing parameters of layer height and flow rate. **(B)–(C)** SEM images of cross-sections printed with different parameters, magnified 20×, scale bar: 200 um. **(D)** Airtightness example and test results at initial air pressures of **(E)** 200 kPa and **(F)** 500 kPa. SEM, scanning electron microscopy.

parallel, continuous, closed-loop paths following the Eulerian path strategy,[38] which is one of the key factors to ensure the airtightness (Supplementary Fig. S9). The top and bottom ends of each printed chamber were sealed using nylon end caps and cyanoacrylate adhesive. Finite element simulations indicated that stresses and strains are generated within the chamber walls under an applied pressure difference, making this design an effective and representative case for assessing whether the optimized printing parameters can reliably achieve airtightness.

To directly assess the effect of optimized printing parameters on the airtightness of the chambers, six examples were fabricated with the chamber's printing layer heights of 0.1 mm, 0.2 mm, and 0.3 mm and extrusion flow rates of 90% and 100%, respectively. The airtightness test was performed by pressurizing each chamber via the pneumatic system, sealing it with a valve, and then measuring the internal pressure changes over time using an air pressure sensor (Supplementary Fig. S10). Each chamber was initially pressurized to 200 kPa, and the pressure retention was monitored over a period of 0–100 s. In this context, a higher retained internal pressure at 100 s indicates better airtightness. As shown in Figure 2E, both layer height and extrusion flow rate directly influence the airtightness of the printed chambers. Specifically, airtightness improves as the layer height decreases and the flow rate increases. When the layer height was set to 0.3 mm, the chambers exhibited poor airtightness: After 100 s, the internal pressure dropped from the initial 200 kPa to only 16.99 kPa (a leakage of 91.51%) and 58.03 kPa (a leakage of 70.99%), respectively. In contrast, reducing the layer height to 0.1 mm significantly enhanced airtightness: After 100 s, the chamber printed with a 90% flow rate retained a pressure of 196.77 kPa (a decrease of only 1.62%), whereas the chamber printed with a 100% flow rate retained 198.29 kPa (a decrease of just 0.85%).

We further evaluated the airtightness of the printed chambers under higher pressure conditions and over an extended duration, as shown in Figure 2F. All four samples maintained internal pressures above approximately 400 kPa even after 10 min, starting from an initial pressure of 500 kPa. Notably, the chamber printed with a layer height of 0.1 mm and an extrusion flow rate of 110% retained a pressure of 462.55 kPa, corresponding to a pressure drop of only about 7.49%. Overall, these results demonstrate that the optimized printing parameter settings can effectively achieve and maintain excellent airtightness. To investigate the trade-offs associated with the over-extrusion strategy, additional experiments examining dimensional accuracy and surface quality were conducted, and the results are summarized in Supplementary Figure S11. Overall, these findings show that combining a moderately increased flow rate with a reduced layer height improves the airtightness and surface finish of the printed chamber walls, while only minimally affecting dimensional accuracy.

3D printing optical waveguides

After successfully fabricating airtight chambers by leveraging the fusibility and flexibility of TPU, this section further explores its flexibility and translucency for the fabrication of optical waveguides. In optical sensors, the primary function of the waveguide is to transmit light from the source to the photodetector. Therefore, we first investigated the light transmittance of the selected TPU filament.

Due to the characteristics of additive manufacturing, the optical performance of printed waveguides is influenced not only by the intrinsic material properties but also by the printing process and the resulting internal microstructure. Previous studies based on SLA printing have shown that the orientation of printed layers can significantly influence optical attenuation, primarily due to differences in curing interfaces and scattering behavior.[32,61] For FDM-printed TPU waveguides, our recent work similarly demonstrated that the printing path introduces orientation-dependent optical behavior.[46] Building upon these findings, the present study further systematically investigates how FDM printing-path orientation affects waveguide transmission performance.

To this end, three rectangular samples (100 × 25 mm × 5 mm) with different printing-path orientations (Supplementary Figs. S12 and S13A) were prepared for transmittance measurements, as illustrated in Figure 3A. In these experiments, light was incident along the *y*-axis, while the printing paths were oriented at 90°, 45°, and 0° relative to the direction of incidence. These samples were fabricated using the slicing strategy shown in Supplementary Figure S13A and Supplementary Table S2, in which the printing angle could be adjusted by setting shells = 0, infill density = 100%, and defining the corresponding infill angle in the slicing software.

Figure 3B presents the transmittance results of the three samples across wavelengths ranging from 350 to 1100 nm. The measurements were performed using an ultraviolet-visible-infrared spectrophotometer (UV-3600 Plus, SHIMADZU) equipped with an integrating sphere (ISR-603). Although all samples share identical dimensions and were fabricated using the same printing process (Supplementary Movie S2), their transmittance differs substantially due to variations in internal microstructure. Specifically, the sample printed with a 0° path orientation achieved an average transmittance of 54.51% within the 550–1100 nm range, whereas the 45° and 90° samples exhibited lower average transmittance values of 33.39% and 24.95%, respectively. The simulation results in Supplementary Figure S14 further confirm that the orientation of internal holes plays a critical role in shaping the optical transmission behavior, as the air holes effectively guide and redirect light within the structure. This behavior is conceptually similar to the guiding mechanism in photonic crystal fibers, where periodically arranged microstructures direct light propagation.[62] Building on these insights, we designed and fabricated waveguides with printing paths aligned parallel to the direction of light propagation. The corresponding printing parameters (layer height = 0.2 mm, flow rate = 100%) are summarized in Supplementary Table S3 and Supplementary Figure S13B, and the resulting internal microstructure is shown in Figure 3C.

Building upon the previous findings regarding FDM printing characteristics and the optical properties of TPU material, we fabricated a bending deformation sensor using a straight optical waveguide with designed dimensions of 4 × 4 × 120 mm. As shown in Figure 3D, this deformation sensor consists of three main components: a commercially available LED and PD, and the printed waveguide. Light emitted by the LED propagates through the waveguide and is subsequently detected by the PD, thereby generating a sensing signal. When the waveguide undergoes bending deformation, its internal light path is disrupted, resulting in increased light leakage. Consequently, variations in the light intensity received by the PD can be correlated with the bending state of the waveguide. For practical applications, the raw sensing signal was converted into a 0–5 V analog voltage using peripheral circuits (Supplementary Fig. S15). An initial demonstration of the sensor's capability is provided in Supplementary Movie S3, in which bending deformations are clearly reflected in the voltage signal.

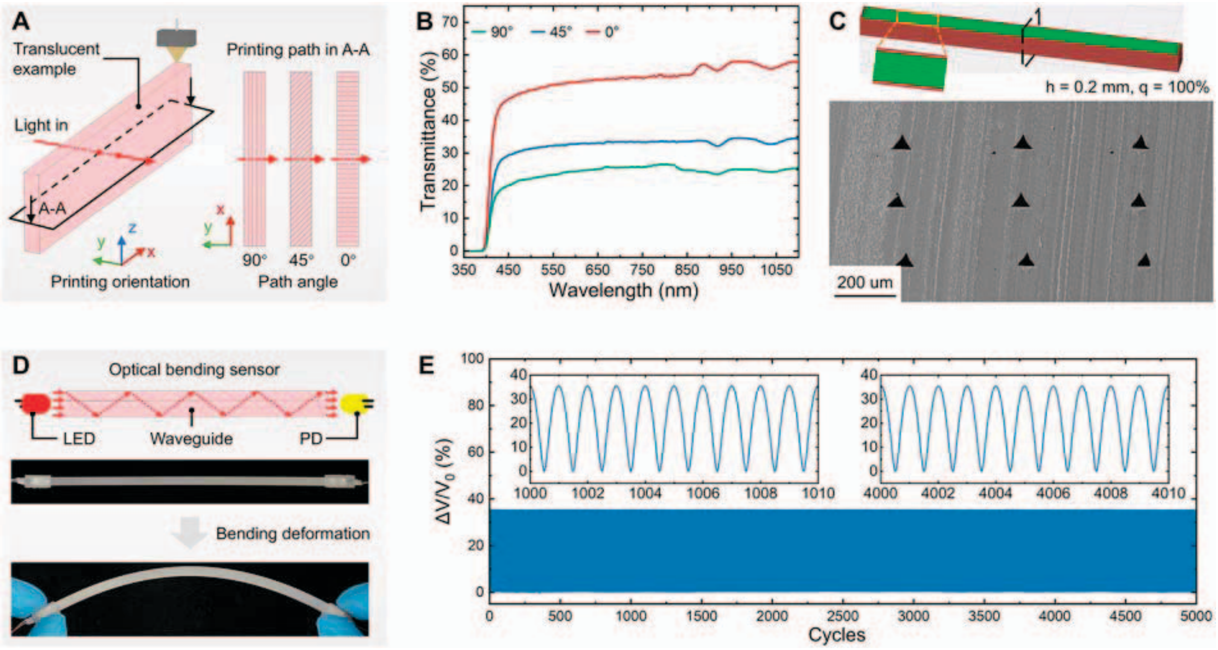

FIG. 3. Light transmission properties of 3D printed waveguides and sensing performance of bending deformation sensors. **(A)** Regulation of transmittance in printed objects through different path designs. **(B)** Transmittance spectra of three sample designs measured across wavelengths from 300 to 1100 nm. **(C)** Slices and internal cross-sections of optical waveguides. **(D)** Structure and working principle of the optical bending sensor. **(E)** Results of the sensor's 5000-cycle bending fatigue test.

To further evaluate the sensor's stability and fatigue resistance, we conducted a repeated bending test at 4 Hz for 5000 cycles using a slider-crank setup (Supplementary Movie S3 and Supplementary Fig. S16). The sensing output is expressed as the voltage change ratio $\Delta V/V_0$, where $\Delta V = V_0 - V$ represents the decrease in voltage relative to the initial value V_0. As shown in Figure 3E, this change ratio remains highly stable throughout the test. In the first cycle, the maximum and minimum values were 0% and 35.50%, respectively, while in the 5000th cycle, they were 0.07% and 35.42%, respectively. This corresponds to a signal drift of only about 0.42%, demonstrating excellent long-term stability. Such robustness provides a strong foundation for the subsequent development of the integrated proprioceptive actuator.

Monolithically printed pneumatic proprioceptive actuators

The core objective of this work is to monolithically fabricate pneumatic proprioceptive actuators through a single-material, single-step printing process. In the previous sections, we analyzed and discussed the airtight pneumatic chambers and optical waveguides separately, both of which are critical components of the proposed MPPPAs. In this section, the actuation and sensing regions are integrated into the combined monolithic design illustrated in Figure 4A (see detailed dimensions in Supplementary Fig. S17) and fabricated monolithically using the slicing strategy shown in Figure 4B. The actuator adopts a classical PneuNet structure,[63] which enables bending actuation, while the optical waveguide is embedded within the bottom constraint layer to effectively capture the overall bending deformation. Under this integrated design, both the actuation and waveguide functional regions of the MPPPA can be monolithically printed as a single seamless structure using group slicing settings in ideaMaker (Supplementary Fig. S18). Supplementary Figure S19 illustrates that this monolithically printed structure exhibits more stable mechanical performance during deformation compared with the assembled structure. Figure 4B shows a fully functional MPPPA that consists of a monolithically printed airtight chamber and optical waveguide, together with an integrated LED and PD, end connectors, and an air inlet. This entire MPPPA features a highly compact design, which is particularly advantageous for robotic applications.

First, we evaluated the basic airtightness performance of the MPPPAs, as shown in Figure 4C, which reports the internal pressure decay over 10 min under initial pressures of 100–500 kPa. The accompanying video (Supplementary Movie S4) partially and visually demonstrates the airtightness performance during the test. At lower pressures, the actuator demonstrates excellent airtightness. For example, starting from 100 kPa, the actuator shows excellent airtightness, with the pressure decreasing by less than 0.1% every 10 s. At higher pressures, airtightness declines slightly (Supplementary Fig. S20), with the 500 kPa case showing an average pressure drop of about 0.68% per 10 s. Overall, the MPPPAs fabricated with the optimized printing parameters can withstand actuation pressures up to 500 kPa while maintaining excellent airtightness. This reliable airtight performance verifies the effectiveness of the proposed airtight-printing strategy and provides a critical foundation for stable pneumatic actuation and consistent proprioceptive sensing in the final monolithic MPPPAs.

After discussing the basic actuation performance of the MPPPAs, we further established a calibration curve based on three devices fabricated with identical printing parameters to evaluate the consistency of their actuation and sensing behaviors and to verify the reliability of the calibration model. These experiments were carried out using the setup shown in Figure 4D, where the pressure input, optical sensing output, and actuator bending angle were simultaneously recorded for subsequent analysis.

For actuation consistency, Figure 4E shows that all three MPPPAs exhibit nearly identical bending responses over the full 0°–300° range, with an average root mean square error (RMSE) of only 0.25°, demonstrating highly consistent mechanical behavior under identical printing conditions. Owing to the characteristics of the PneuNet structure, the actuator exhibits distinct deformation regimes before and after chamber-wall contact; therefore, similar to the sensing calibration, a third-order polynomial was used to fit the bending-pressure relationship, with the fitted model provided in Note S3. The fitted curve achieved an average RMSE of 0.71° across the three datasets, confirming both the accuracy and robustness of the calibration. Supplementary Note S2 and Supplementary Figure S21 further confirm that embedding the optical waveguide does not appreciably compromise the actuator's mechanical performance, while simultaneously enabling proprioceptive sensing capability.

For sensing consistency, slight variations are observed in the raw data (Supplementary Fig. S22), likely resulting from small assembly deviations during manual LED/PD installation and minor printing differences in the internal waveguide microstructure. After applying [0,1] normalization, the bending-sensing curves (angle-ΔV_{norm}) in Figure 4F exhibit strong agreement across all three MPPPAs. Based on the comprehensive fitting error analysis in Supplementary Table S4, a third-order polynomial was used to model the proprioceptive sensing behavior of the MPPPAs, with the fitted expression provided in Note S3. The model achieved an average RMSE of 2.01° (3.35%) across the three datasets, confirming that the optical sensing response remains highly consistent after normalization. This calibrated sensing model is subsequently used for all proprioceptive functions demonstrated in the later applications of the MPPPAs.

After characterizing the basic actuation and sensing performance of the MPPPAs, we next investigate their proprioceptive capabilities. In conventional SPAs, internal air pressure signals are often used to infer the actuation state. However, due to the inherent hysteresis of soft materials, this approach can introduce delays in the actuator's response, as illustrated in Figure 4G. Specifically, when the internal air pressure changes rapidly, for example, dropping from 300 to 0 kPa within 1 s, the soft actuator cannot immediately return to its original horizontal posture. This makes it challenging to accurately estimate its proprioceptive state based solely on pressure data. In contrast, the proposed MPPPAs leverage continuous structural integration and uniform mechanical properties across the actuator and sensing regions, enabling real-time feedback of deformation through optical sensing signals. To validate this capability, we performed five cyclic bending tests on the MPPPAs and compared the bending angles estimated using an air pressure sensor with those measured by the integrated optical waveguide sensor. The comparison results are shown in Figure 4H, where the

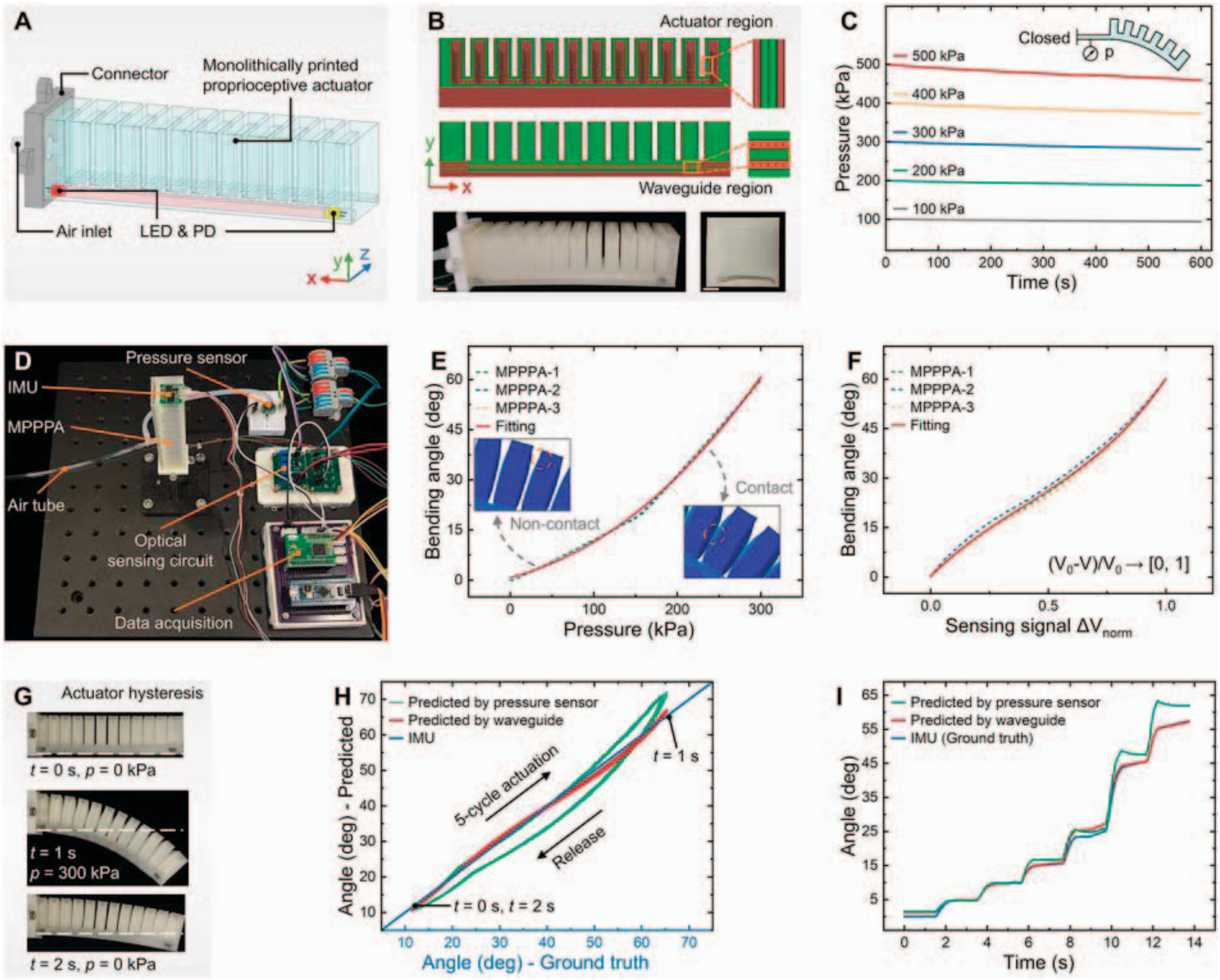

FIG. 4. Monolithically printed proprioceptive actuator and its proprioceptive performance. **(A)** Overall structure and components of the MPPPA. **(B)** Sliced and printed MPPPA (scale bar: 5 mm). **(C)** Long-term airtightness performance of the MPPPAs. **(D)** Experimental setup used for calibration and testing of the actuator's proprioceptive sensing. **(E)** Deformation behavior of three MPPPA samples with identical printing parameters under pneumatic actuation. **(F)** Calibration curve demonstrating the relationship between actuator deformation and waveguide-based sensing signal. **(G)** Soft actuators inherently exhibit hysteresis during actuation cycles. **(H)** Comparison between pressure-based sensing and waveguide-based proprioception. **(I)** Proprioceptive response of the MPPPA under continuous step-pressure inputs.

horizontal axis indicates bending angles obtained from an inertial measurement unit sensor, considered as the ground truth, and the vertical axis shows the predicted angles. As observed, the angles predicted based on internal air pressure (green curve) exhibit pronounced hysteresis, resulting in an RMSE of 3.27° relative to the actual angles. In contrast, the angles predicted by the optical waveguide (red curve) demonstrate better repeatability and consistency, closely aligning with the 45° reference line and yielding a lower RMSE of just 0.92°.

Additionally, we further compared the proprioceptive performance of the internal air pressure sensor and the integrated optical waveguide under a stepwise actuation response, as shown in Figure 4I. This experiment was designed to evaluate the proprioceptive sensing capability of the MPPPA under dynamic actuation and hysteresis conditions, where SPAs typically exhibit delayed mechanical responses due to the viscoelasticity of the material. Such hysteresis often leads to notable discrepancies when actuator posture is inferred solely from internal pressure measurements.

In contrast, in the proposed MPPPAs, both the actuator and the optical waveguide regions are monolithically fabricated from the same TPU material, ensuring identical mechanical properties and synchronized deformation. Therefore, the optical waveguide-based sensing can more accurately capture the actuator's true deformation during dynamic actuation.

In this experiment, the performances of the above proprioception methods based on air pressure signals and optical waveguide signals were comparatively analyzed under MPPPA actuation from 0° to 55°. The results show that the RMSE of the bending angle predicted using the internal air pressure sensor was 2.91°, whereas that obtained using the integrated optical waveguide was only 1.00° (approximately 1.82%), confirming the superior proprioceptive accuracy and reliability of the proposed MPPPAs under dynamic and hysteretic conditions.

In summary, these results demonstrate that the proposed monolithically 3D printed pneumatic proprioceptive actuator exhibits excellent actuation performance and superior proprioceptive sensing capability. In the following section, we further investigate practical applications to fully exploit its integrated sensing functionality.

Demonstrations on surface contour and gripping width measurement

In this section, the highly integrated, self-sensing MPPPA is first employed for surface contour measurement to demonstrate its proprioceptive sensing capabilities. As shown in Figure 5A, the experimental setup consists of the MPPPA bending to press against the target surface, while a motor-driven horizontal stage enables it to slide along the surface and detect its contour (Supplementary Movie S5). The model underlying this setup is illustrated in Figure 5B, where the bending of the MPPPA is approximated as a constant-curvature deformation. Based on this assumption, the surface-contour reconstruction model leveraging the MPPPA's proprioceptive sensing capability is provided in Note S4. In this model, $s = 86.5$ mm is the length of the actuator's constraint layer, θ is the bending angle, r is the corresponding bending radius, y_0 25.5 mm represents the initial offset distance between the MPPPA and the surface in our experimental setup. Consequently, by continuously recording h as the sliding distance x increases, the complete surface contour can thus be measured.

The initial installation vertical position of the MPPPA tip was $y_0 = 25.5$ mm. According to Equations (S4–S6), when the MPPPA bends by 34.84° under an actuation pressure of 199.6 kPa, its tip just contacts the target surface. To ensure stable contact during the scanning process, the MPPPA was inflated to 200 kPa and then sealed for all three surface contour detection trials.

During the experiments, the MPPPA and its mounting platform were driven to move horizontally at a constant velocity of 3 mm/s. As the actuator slid over the target surface, its bending angle varied in response to the surface height and contact force. These variations were captured by the embedded optical waveguide sensor in real time, enabling reconstruction of the surface contour. The horizontal displacement and corresponding sensing signals were simultaneously recorded and used for quantitative surface contour reconstruction.

This measurement was conducted on five surface samples representing three distinct geometries, including arc, slope, and sawtooth shapes, and maximum heights of 3 mm, 1 mm, and 0.5 mm, respectively (Supplementary Fig. S23), using the setup shown in Supplementary Figure S24.

Figure 5C presents three measurement results, which include both the reference surface contours of the target objects (blue curves) and the experimentally reconstructed contours (red curves). For the surface with a height of 3 mm, the reconstructed and reference curves show good agreement, indicating high reconstruction accuracy. Specifically, the arc-shaped surface, composed of three continuous arcs, achieved an RMSE of 0.16 mm. For the sloped surface, measurement accuracy decreased near the sharp corner around $x = 100$ mm, leading to an overall RMSE of 0.33 mm. For the 3 mm high sawtooth surfaces, which contain nine sawtooth features, the overall contour was captured but with larger deviations, resulting in an RMSE of 0.48 mm.

Finer surface contours were also evaluated, including sawtooth structures with heights of 1 mm and 0.5 mm, as shown in Figure 5D. The former consisted of 25 sawtooth units, and the latter of 50 units. The results show that although the MPPPA could still capture the general shapes of these finer features via proprioceptive sensing, deviations were more pronounced. The RMSE values for these tests were 0.27 mm (27%) and 0.12 mm (24%), respectively. These increased errors are partly attributed to the rounding of sharp corners on the test surfaces, which were also produced by 3D printing with PLA material.

To further explore the application potential of the proposed MPPPAs, we assembled two actuators into a soft proprioceptive gripper, as illustrated in Figure 5E. By leveraging the integrated proprioceptive sensing capability of the MPPPAs and Equation (S6), the gripper can estimate the fingertip gripping width d using the Equation (S7) in Note S4.

Based on the gripper geometry and Equation (S7), when each MPPPA bends by 48.02° under an actuation pressure of 244.01 kPa, the fingertip width becomes $d = 0$ mm. To ensure continuous contact between the gripper and the target object during the entire experiment, each MPPPA was inflated to 250 kPa and then sealed.

During the experiment, the target object and its mounting platform moved horizontally at a constant velocity of 1 mm/s. As the gripper slid along the object surface, its fingertip angle varied in response to the local surface height and contact force, as shown in Supplementary Figure S25. These variations were captured in real time by the embedded optical waveguide sensors, enabling reconstruction of both the object width and contour. The horizontal displacement and corresponding optical sensing signals were simultaneously recorded for quantitative shape and width reconstruction.

The experimental results are presented in Figure 5F, which show that the proprioceptive data successfully captured both the object contours and the gripper's dynamic gripping width. As illustrated in the figure, the overall shapes and widths of the pen and the bit (blue curves) were well reproduced by the proprioceptive gripper (red curves). The reconstructed width profiles achieved an RMSE of approximately 0.68 mm for the pen (about 6.8% of its maximum width) and 0.53 mm for the bit (about 8.4% of its maximum width).

However, as shown in the two error plots at the bottom of Figure 5F, some localized deviations remain, particularly at discontinuous width transitions along the object surfaces. For instance, the maximum reconstruction error reached approximately 2.25 mm at the step region of the pen and 2.78 mm at that of the bit. These errors primarily arise because the proprioceptive actuators cannot instantaneously adapt to abrupt changes in surface geometry during motion, leading to transient discrepancies in the reconstructed profiles.

Overall, by utilizing proprioceptive feedback from the embedded optical waveguides, the compact and rapidly fabricated gripper effectively detects object shapes and contours, demonstrating strong potential for broader applications in dexterous grasping and object recognition.

Discussion and Conclusions

This article presents a design and fabrication method to MPPPAs that integrate actuation and sensing capabilities within a single soft body, inspired by the structure and proprioceptive mechanism of human muscle tissue. By leveraging the multifunctional properties of a single TPU material, specifically its flexibility, fusibility, and translucency, we

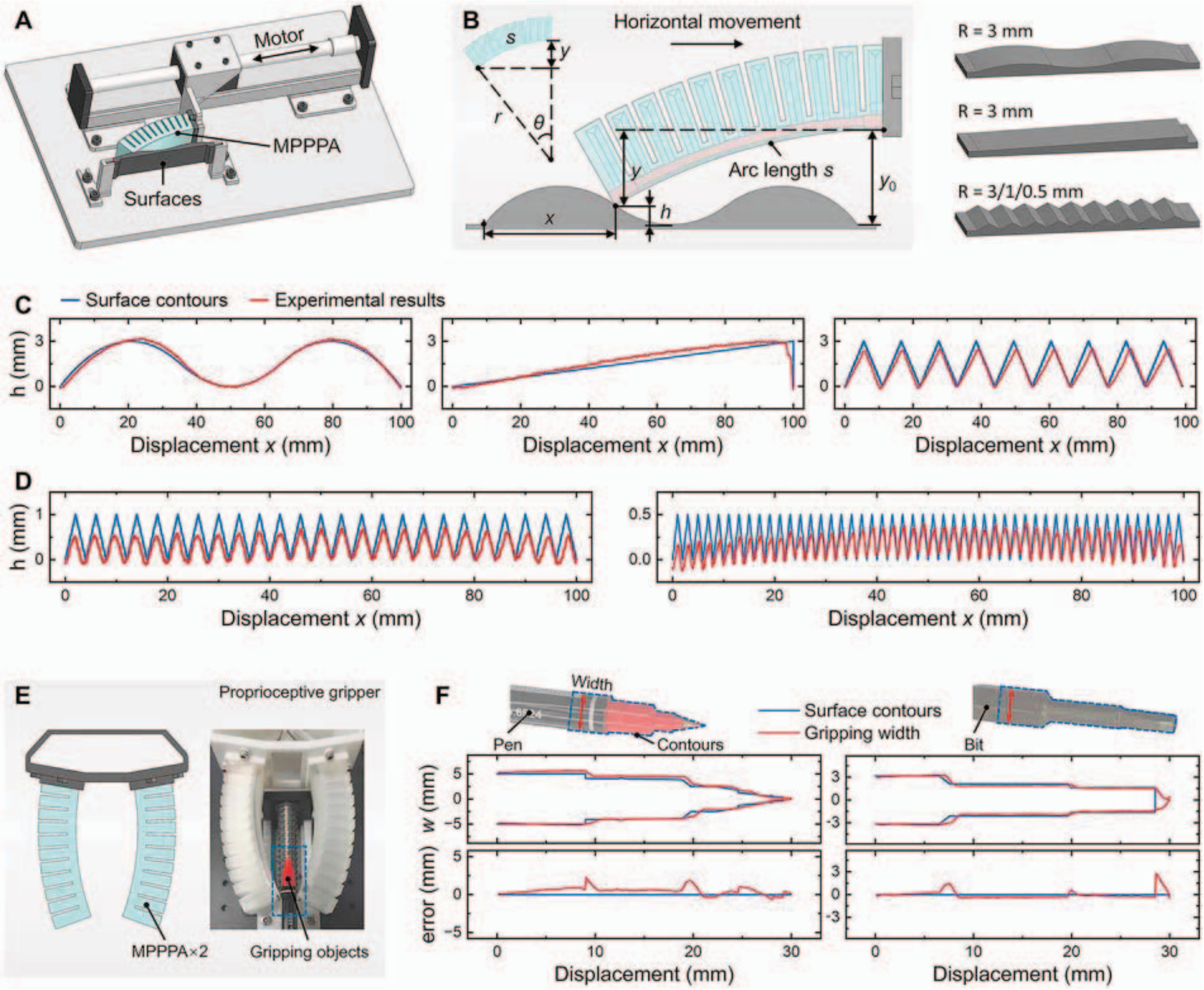

FIG. 5. Demonstrations of the surface contour reconstruction and gripping width measurement. **(A)** Experimental setup for surface contour reconstruction. **(B)** Schematic illustration of the sensing model for three types of surface contours. **(C)** and **(D)** Reconstructed sensing results for surfaces with roughness amplitudes of 3, 1, and 0.5 mm, respectively. **(E)** Structure of the proprioceptive gripper composed of two MPPPA units. **(F)** The proprioceptive gripper measures its gripping width and the surface contours of two objects.

successfully fabricated airtight actuator chambers for reliable motion generation and embedded optical waveguides for proprioceptive sensing, using a conventional desktop-level FDM printer. The proposed monolithic design fundamentally avoids issues caused by mismatched mechanical properties in multimaterial integration and ensures continuous structural integration between actuation and sensing regions, thereby maintaining synchronized deformations and enhancing overall robustness.

To realize integrated actuation and sensing, we systematically investigated 3D printing airtight chambers, showing that optimizing printing parameters can significantly reduce internal porosity. Specifically, by decreasing the layer height to 0.1 mm and increasing the extrusion flow rate to 110%, the printed chambers achieved a dense internal structure entirely free of air holes, as confirmed by SEM imaging. These chambers maintained high internal pressures, retaining 462.55 kPa after 10 min from an initial 500 kPa, corresponding to only a 7.49% pressure drop, demonstrating excellent airtightness and reliable actuation capability. We then explored the fabrication of optical waveguides using the same TPU material by leveraging its inherent flexibility and translucency, along with optimized toolpaths and printing parameters. Experimental results demonstrated that incorporating parallel air holes adjacent to the optical waveguide significantly reduced light attenuation, thereby enhancing transmission efficiency. The fabricated optical waveguide sensor exhibited stable signal output over 5000 consecutive bending cycles at 4 Hz, with a minimal signal drift of only 0.4% over time, confirming its robustness and reliability for real-time proprioceptive sensing feedback.

Building on the development of 3D printed chambers and optical waveguides, we then achieved the monolithic fabrication of MPPPAs through a single uninterrupted printing process using a single material by means of an integrated actuator-sensor design and parameter optimization. Mechanical tests confirmed high structural integrity and mechanical robustness of the monolithically printed actuator-sensor region, with a measured peel force of 93.96 N and tensile strength of 42.95 MPa. The resulting MPPPAs exhibited excellent actuation and sensing performance, with an average leakage rate of approximately 0.68% every 10 seconds under 500 kPa, and a proprioceptive sensing error of less than 1.82% during actuation. This highly integrated, proprioceptively stable, and easily fabricated MPPPA was employed in a surface measurement demonstration, achieving RMSE as low as 0.16 mm for arc-shaped surfaces with heights up to 3 mm, and 0.27 mm for sawtooth surfaces with heights up to 1 mm. Furthermore, two MPPPAs were integrated into a soft proprioceptive gripper, demonstrating its capability for real-time estimation of gripping width and accurate object contour detection.

These experimental results prove that the proposed MPPPA enables the efficient fabrication of compact pneumatic proprioceptive actuators with stable mechanical and sensing integration. This approach paves the way for advancing soft robotic systems featuring enhanced proprioceptive capabilities alongside streamlined manufacturing processes.

Future work will focus on further integrating and expanding the multimodal capabilities of both sensing and actuation within MPPPAs to realize a fully unified multimodal proprioceptive actuator. We will also systematically investigate and optimize printing parameters to achieve complete airtightness of the actuators under high-pressure conditions. Moreover, leveraging the stable proprioceptive feedback from MPPPAs, we aim to develop advanced closed-loop control algorithms to enable intelligent and precise robotic motion and interaction. Ultimately, these efforts will facilitate the deployment of MPPPAs in intelligent soft robotic systems capable of adaptive and autonomous operation in complex, unstructured environments.

Authors' Contributions

S.T.: Conceptualization, methodology, investigation, visualization, writing—original draft, and writing—review and editing. X.L.: Methodology, software, and formal analysis. Z.F.: Methodology and investigation. Y.W.: Validation. J.Y.: Methodology, and supervision. Z.W.: Conceptualization. J.D.: Supervision. S.L.: Conceptualization, supervision, funding acquisition, and writing—review and editing.

Data Availability

The data that support the findings of this study are available within the main text and the supplementary information. All data are also available from the corresponding authors upon reasonable request.

Author Disclosure Statement

The authors declare that they have no competing financial interests.

Funding Information

This work was partly supported by the National Natural Science Foundation of China (Grant 52475302), National Key R&D Program of China (Grant No. 2022YFB4701200), Shenzhen Science and Technology Program (Grant JCYJ20220530114615034 and JCYJ20220818100417038), and Guangdong Provincial Key Laboratory of Intelligent Morphing Mechanisms and Adaptive Robotics (Grant 2023B1212010005).

Supplementary Material

Supplementary Data
Supplementary Movie S1
Supplementary Movie S2
Supplementary Movie S3
Supplementary Movie S4
Supplementary Movie S5

References

1. Xavier MS, Tawk CD, Zolfagharian A, et al. Soft pneumatic actuators: A review of design, fabrication, modeling, sensing, control and applications. IEEE Access 2022;10:59442–59485; doi: 10.1109/ACCESS.2022.3179589
2. Walker J, Zidek T, Harbel C, et al. Soft robotics: A review of recent developments of pneumatic soft actuators. Actuators 2020;9(1):3; doi: 10.3390/act9010003
3. Whitesides GM. Soft robotics. Angew Chem Int Ed Engl 2018;57(16):4258–4273; doi: 10.1002/anie.201800907
4. Tang Y, Chi Y, Sun J, et al. Leveraging elastic instabilities for amplified performance: Spine-inspired high-speed and high-force soft robots. Sci Adv 2020;6(19):eaaz6912; doi: 10.1126/sciadv.aaz6912
5. Wu Y, Huang N, Tang S, et al. A multi-facet-effector soft robot in polyhedral configuration for multidirectional function reuse. Mech Mach Theory 2025;217:106240; doi: 10.1016/j.mechmachtheory.2025.106240
6. Liu S, Zhu Y, Zhang Z, et al. Otariidae-inspired soft-robotic supernumerary flippers by fabric Kirigami and Origami. IEEE/ASME Trans Mechatron 2021;26(5):2747–2757; doi: 10.1109/TMECH.2020.3045476
7. Polygerinos P, Wang Z, Galloway KC, et al. Soft robotic glove for combined assistance and at-home rehabilitation. Rob Auton Syst 2015;73:135–143; doi: 10.1016/j.robot.2014.08.014
8. Wang H, Totaro M, Beccai L. Toward perceptive soft robots: Progress and challenges. Adv Sci (Weinh) 2018;5(9):1800541; doi: 10.1002/advs.201800541
9. Wang L, Lam J, Chen X, et al. Soft robot proprioception using unified soft body encoding and recurrent neural network. Soft Robot 2023;10(4):825–837; doi: 10.1089/soro.2021.0056
10. Zhou S, Li Y, Wang Q, et al. Integrated actuation and sensing: Toward intelligent soft robots. Cyborg Bionic Syst 2024;5:0105; doi: 10.34133/cbsystems.0105
11. Ji Q, Zhang X, Chen M, et al. Design and closed loop control of a 3D printed soft actuator. In: 2020 IEEE 16th International Conference on Automation Science and Engineering (CASE) IEEE: Hong Kong, Hong Kong; 2020; pp. 842–848; doi: 10.1109/CASE48305.2020.9216946
12. Rus D, Tolley MT. Design, fabrication and control of soft robots. Nature 2015;521(7553):467–475; doi: 10.1038/nature14543
13. Tapia J, Knoop E, Mutný M, et al. MakeSense: Automated sensor design for proprioceptive soft robots. Soft Robot 2020;7(3):332–345; doi: 10.1089/soro.2018.0162
14. Faris O, Muthusamy R, Renda F, et al. Proprioception and exteroception of a soft robotic finger using neuromorphic vision-based sensing. Soft Robot 2023;10(3):467–481; doi: 10.1089/soro.2022.0030
15. Gerboni G, Diodato A, Ciuti G, et al. Feedback control of soft robot actuators via commercial flex bend sensors.

IEEE/ASME Trans Mechatron 2017;22(4):1881–1888; doi: 10.1109/tmech.2017.2699677

16. Su Y, Chen X, Fang Z, et al. Spatial position–force perception for a soft parallel joint via pressure-deformation self-sensing. IEEE/ASME Trans Mechatron 2024;29(5):3590–3601; doi: 10.1109/tmech.2023.3340342
17. Wu S, Tang K, Tang S, et al. High-performance hydraulic soft robotic control using continuous flow regulation and partial feedback. IEEE Robot Autom Lett 2024;9(8): 6967–6974; doi: 10.1109/lra.2024.3416770
18. Tang S, Tang K, Wu S, et al. Performance enhancement of the soft robotic segment for a trunk-like arm. Front Robot AI 2023;10:1210217; doi: 10.3389/frobt.2023.1210217
19. Wang L, Wang Z. Mechanoreception for soft robots via intuitive body cues. Soft Robot 2020;7(2):198–217; doi: 10.1089/soro.2018.0135
20. Liu W, Duo Y, Chen X, et al. An intelligent robotic system capable of sensing and describing objects based on bimodal, self-powered flexible sensors. Adv Funct Materials 2023; 33(41); doi: 10.1002/adfm.202306368
21. Qu J, Cui G, Li Z, et al. Advanced flexible sensing technologies for soft robots. Adv Funct Materials 2024;34(29); doi: 10.1002/adfm.202401311
22. Yi Z, Gong S, Fang F, et al. Sensor-actuator integration for intelligent devices. Device 2025;3(4):100717; doi: 10.1016/j.device.2025.100717
23. Gariya N, Kumar S, Shaikh A, et al. A review on soft pneumatic actuators with integrated or embedded soft sensors. Sensors and Actuators A: Physical 2024;372:115364; doi: 10.1016/j.sna.2024.115364
24. Wang S, Sun Z, Zhao Y, et al. A highly stretchable hydrogel sensor for soft robot multi-modal perception. Sensors and Actuators A: Physical 2021;331:113006; doi: 10.1016/j.sna.2021.113006
25. Dai X, Wu Y, Liang Q, et al. Soft robotic-adapted multimodal sensors derived from entirely intrinsic self-healing and stretchable cross-linked networks. Adv Funct Materials 2023;33(44); doi: 10.1002/adfm.202304415
26. Liu L, Huang X, Zhang X, et al. Model-based 3D shape reconstruction of soft robots via distributed strain sensing. Soft Robot 2025;12(6):721–731; doi: 10.1089/soro.2024.0158
27. Wang Z, Polygerinos P, Overvelde JTB, et al. Interaction forces of soft fiber reinforced bending actuators. IEEE/ASME Trans Mechatron 2017;22(2):717–727; doi: 10.1109/tmech.2016.2638468
28. Galloway KC, Chen Y, Templeton E, et al. Fiber optic shape sensing for soft robotics. Soft Robot 2019;6(5): 671–684; doi: 10.1089/soro.2018.0131
29. Mo L, Zhang D, Fu X, et al. A multidirectional external perception soft actuator based on flexible optical waveguide for underwater teleoperation. Advanced Intelligent Systems 2023;5(10); doi: 10.1002/aisy.202300029
30. Zhao H, O'Brien K, Li S, et al. Optoelectronically innervated soft prosthetic hand via stretchable optical waveguides. Sci Robot 2016;1(1):eaai7529; doi: 10.1126/scirobotics.aai7529
31. Yi J, Kim B, Cho K-J, et al. Underactuated robotic gripper with fiber-optic force sensing tendons. IEEE Robot Autom Lett 2023;8(11):7607–7614; doi: 10.1109/LRA.2023.3315204
32. Trunin P, Cafiso D, Beccai L. Design and 3D printing of soft optical waveguides towards monolithic perceptive systems. Addit Manuf 2025;100:104687; doi: 10.1016/j.addma.2025.104687
33. Baines R, Zuliani F, Chennoufi N, et al. Multi-modal deformation and temperature sensing for context-sensitive machines. Nat Commun 2023;14(1):7499; doi: 10.1038/s41467-023-42655-y
34. Kim T, Lee S, Hong T, et al. Heterogeneous sensing in a multifunctional soft sensor for human-robot interfaces. Sci Robot 2020;5(49):eabc6878; doi: 10.1126/scirobotics.abc6878
35. Zhao Y, Lo C-Y, Ruan L, et al. Somatosensory actuator based on stretchable conductive photothermally responsive hydrogel. Sci Robot 2021;6(53):eabd5483; doi: 10.1126/scirobotics.abd5483
36. Xue P, Valenzuela C, Ma S, et al. Highly conductive MXene/PEDOT:PSS-integrated poly (*N* -Isopropylacrylamide) hydrogels for bioinspired somatosensory soft actuators. Adv Funct Materials 2023;33(24):2214867; doi: 10.1002/adfm.202214867
37. Yu KY, Kim H, Lee IH. Multi-material additive manufacturing process design of sensor embedded soft gripper. Sensors and Actuators A: Physical 2025;386:116322; doi: 10.1016/j.sna.2025.116322
38. Gul JZ, Sajid M, Rehman MM, et al. 3D printing for soft robotics – A review. Sci Technol Adv Mater 2018;19(1): 243–262; doi: 10.1080/14686996.2018.1431862
39. Sachyani Keneth E, Kamyshny A, Totaro M, et al. 3D printing materials for soft robotics. Adv Mater 2021;33(19): e2003387; doi: 10.1002/adma.202003387
40. Yi J, Chen X, Song C, et al. Customizable three-dimensional-printed Origami soft robotic joint with effective behavior shaping for safe interactions. IEEE Trans Robot 2019;35(1):114–123; doi: 10.1109/tro.2018.2871440
41. Zhai Y, De Boer A, Yan J, et al. Desktop fabrication of monolithic soft robotic devices with embedded fluidic control circuits. Sci Robot 2023;8(79):eadg3792; doi: 10.1126/scirobotics.adg3792
42. Zhang Y, Zhang N, Hingorani H, et al. Fast-response, stiffness-tunable soft actuator by hybrid multimaterial 3D printing. Adv Funct Materials 2019;29(15); doi: 10.1002/adfm.201806698
43. Ali M, Hu C, Yttri EA, et al. Recent advances in 3D printing of biomedical sensing devices. Adv Funct Mater 2022; 32(9):2107671; doi: 10.1002/adfm.202107671
44. Li C, Cheng J, He Y, et al. Polyelectrolyte elastomer-based ionotronic sensors with multi-mode sensing capabilities via multi-material 3D printing. Nat Commun 2023;14(1):4853; doi: 10.1038/s41467-023-40583-5
45. Tang S, Tang K, Guo Y, et al. Soft robotic proprioception enhancement via 3D-printed differential optical waveguide design. IEEE Robot Autom Lett 2024;9(8):6975–6982; doi: 10.1109/LRA.2024.3416795
46. Li Y, Wu Z, Chen Y, et al. Multi-material embedded 3D printing for one-step manufacturing of multifunctional components in soft robotics. Addit Manuf 2024;85:104178; doi: 10.1016/j.addma.2024.104178
47. Lalegani Dezaki M, Sales R, Zolfagharian A, et al. Soft pneumatic actuators with integrated resistive sensors enabled by multi-material 3D printing. Int J Adv Manuf Technol 2023;128(9–10):4207–4221; doi: 10.1007/s00170-023-12181-8
48. Mousavi S, Howard D, Zhang F, et al. Direct 3D printing of highly anisotropic, flexible, constriction-resistive sensors for multidirectional proprioception in soft robots. ACS Appl

Mater Interfaces 2020;12(13):15631–15643; doi: 10.1021/acsami.9b21816

49. Shorthose O, Albini A, He L, et al. Design of a 3D-printed soft robotic hand with integrated distributed tactile sensing. IEEE Robot Autom Lett 2022;7(2):3945–3952; doi: 10.1109/lra.2022.3149037
50. Truby RL, Wehner M, Grosskopf AK, et al. Soft somatosensitive actuators via embedded 3D printing. Adv Mater 2018;30(15):e1706383; doi: 10.1002/adma.201706383
51. Xian S, Xu Y, Li Y, et al. Flexible triboelectric sensor based on catalyst-diffusion self-encapsulated conductive liquid-metal-silicone ink for somatosensory soft robotic system. Adv Funct Materials 2025;35(2); doi: 10.1002/adfm.202412293
52. Fang Z, Tang S, Su Y, et al. 3D printed multi-cavity soft actuator with integrated motion and sensing functionalities via bioinspired interweaving foldable endomysium. Adv Sci (Weinh) 2025;12(3):e2409060; doi: 10.1002/advs.202409060
53. Jerosch J, Prymka M. Proprioception and joint stability. Knee Surg Sports Traumatol Arthrosc 1996;4(3):171–179; doi: 10.1007/BF01577413
54. Tuthill JC, Azim E. Proprioception. Curr Biol 2018;28(5): R194–R203; doi: 10.1016/j.cub.2018.01.064
55. Derrickson BH, Tortora GJ. Tortora's Principles of Anatomy & Physiology. [15th ed.]. Wiley: Danvers MA; 2017.
56. Purslow PP. The structure and functional significance of variations in the connective tissue within muscle. Comp Biochem Physiol A Mol Integr Physiol 2002;133(4):947–966; doi: 10.1016/s1095-6433(02)00141-1
57. Purslow PP. The structure and role of intramuscular connective tissue in muscle function. Front Physiol 2020;11:495; doi: 10.3389/fphys.2020.00495
58. Ritzen L, Montano V, Garcia SJ. 3D printing of a self-healing thermoplastic polyurethane through FDM: From polymer slab to mechanical assessment. Polymers (Basel) 2021;13(2):305; doi: 10.3390/polym13020305
59. Yin J, Lu C, Fu J, et al. Interfacial bonding during multi-material fused deposition modeling (FDM) process due to inter-molecular diffusion. Materials & Design 2018;150: 104–112; doi: 10.1016/j.matdes.2018.04.029
60. Zhai Y, Yan J, De Boer A, et al. Monolithic desktop digital fabrication of autonomous walking robots. Advanced Intelligent Systems 2025;7(5):2400876; doi: 10.1002/aisy.202400876
61. Alam F, Elsherif M, Salih AE, et al. 3D printed polymer composite optical fiber for sensing applications. Addit Manuf 2022;58:102996; doi: 10.1016/j.addma.2022.102996
62. Russell P. Photonic crystal fibers. Science 2003;299(5605): 358–362; doi: 10.1126/science.1079280
63. Mosadegh B, Polygerinos P, Keplinger C, et al. Pneumatic networks for soft robotics that actuate rapidly. Adv Funct Materials 2014;24(15):2163–2170; doi: 10.1002/adfm.201303288

Address correspondence to:
Sicong Liu
Sino-German College of Intelligent Manufacturing
Shenzhen Technology University
3002 Lantian Rd.
Pingshan District
Shenzhen, Guangdong
China

E-mail: liusicong@sztu.edu.cn